


Research Article

The Synchronization of Electron Enricher and Electron Extractor as Ternary Composite Photoanode for Enhancement of DSSC Performance

Weradesh Sangkhun,¹ Sompit Wanwong,^{1,2} Nutthapon Wongyao,³ Teera Butburee,⁴ Pisist Kumnorkaew,⁴ and Jatuphorn Wootthikanokkhan ^{1,2}

¹Materials Technology Program, School of Energy, Environment and Materials, King Mongkut's University of Technology Thonburi (KMUTT), 126 Pracha Uthit Rd., Bang Mod Thung Khru, Bangkok 10140, Thailand

²Nanotec-KMUTT Center of Excellence on Hybrid Nanomaterials for Alternative Energy (HyNAE), School of Energy, Environment and Materials, King Mongkut's University of Technology Thonburi, 126 Pracha Uthit Rd., Bang Mod Thung Khru, Bangkok 10140, Thailand

³Fuel Cells and Hydrogen Research and Engineering Center, King Mongkut's University of Technology Thonburi, 126 Pracha Uthit Rd., Bang Mod Thung Khru, Bangkok 10140, Thailand

⁴National Nanotechnology Center, National Science and Technology Development Agency, Thailand Science Park, Pathum Thani 12120, Thailand

Correspondence should be addressed to Jatuphorn Wootthikanokkhan; jatuphorn.woo@kmutt.ac.th

Received 2 January 2020; Accepted 19 February 2020; Published 16 March 2020

Guest Editor: Abdelrahman Zkria

Copyright © 2020 Weradesh Sangkhun et al. This is an open access article distributed under the Creative Commons Attribution License, which permits unrestricted use, distribution, and reproduction in any medium, provided the original work is properly cited.

This work developed a novel ternary composite photoanode of dye-sensitized solar cell (DSSC) composed of (i) N-, S-doped titanium dioxide with exposed {001} facet (N-, S-TiO_{2{001}}), (ii) N-, S-doped reduced graphene oxide (N-, S-rGO), and (iii) commercial titanium dioxide (P25). The DSSC device fabricated with the ternary composite photoanode showed the greatest of power conversion efficiency (8.62%) compared to the device fabricated with P25 photoanode (3.20%). This enhancement was attributed to the synergistic effect of the N-, S-TiO_{2{001}} and the N-, S-rGO, which act as an electron enricher and an electron extractor, respectively.

1. Introduction

Dye-sensitized solar cell (DSSC) has gained a considerable attention as a potential solar device. The performance of the DSSC could be improved by several strategies, including the development of more efficient dye sensitizers [1, 2] electrolyte systems [3], counter electrodes [4, 5], and photoanodes [6, 7]. Among these, the photoanode is an integral part determining the overall efficiency of DSSC because it has strong influence on dye adsorption ability and charge transport properties [8, 9]. However, the commonly used photoanode material such as titanium dioxide P25 still has

some drawbacks, including large bandgap energy (BGE) and low electron (e⁻) mobility, resulting in low power conversion efficiency (PCE) of devices [10]. In this regard, an inclusion of TiO₂ with exposed {001} facet (TiO_{2{001}}) as a 2D material into the photoanode systems was reported that can significantly enhance charge transport [11, 12]. In addition, the electronic properties of TiO_{2{001}} can be easily tuned by doping with nonmetallic atoms to improve light harvesting efficiency [13, 14]. However, this might also lead to the formation of deep trap state, which induces the charge recombination [15]. To cope up with this problem, the use of nonmetallic atom-doped reduced graphene oxide (rGO)

is of our interest because of its high conductivity to quickly extract the photoexcited e^- before the recombination could take place [16–18].

In this work, we introduce an alternative approach to enhance DSSC performance using a novel ternary composite photoanode based on N-, S-doped $\text{TiO}_{2\{001\}}$, N-, S-doped rGO, and P25. First, the N-, S-doped $\text{TiO}_{2\{001\}}$ and N-, S-doped rGO were synthesized and optimized. The effect of mixing ratios between N-, S-doped $\text{TiO}_{2\{001\}}$ and/or N-, S-doped rGO in P25 on performance of the DSSC was also investigated. The mechanism behind a synergistic effect of the ternary composite photoanode was elucidated by using ultraviolet-visible (UV-vis) spectroscopy, photoluminescence spectroscopy (PL), external quantum efficiency (EQE), and electrochemical impedance spectroscopy (EIS).

2. Results and Discussion

$\text{TiO}_{2\{001\}}$ was synthesized by hydrothermal technique. More details can be found in Supplementary Information (SI) S1.1 and S1.2. The morphology of various $\text{TiO}_{2\{001\}}$ was observed by scanning electron microscope (SEM). It was found that when HF concentration was increased, the thickness of $\text{TiO}_{2\{001\}}$ particles was decreased, while the lateral size of particles increased (Figures 1(a)–1(c)). This result is in agreement with our recent report [19]. In addition, the platelet $\text{TiO}_{2\{001\}}$ particles were transformed to a hierarchical sheet-like structure and tended to aggregate, forming stacked hierarchical particles when HF/Ti ratio was reached to 3 and 4, respectively (Figures 1(c) and 1(d)).

Figure 1(e) showed that the X-ray diffraction patterns of all $\text{TiO}_{2\{001\}}$ samples were perfectly indexed as anatase (JCPDS card no. 21-1272). Furthermore, as shown in Figure 1(g), the percentage of {001} facet (%S) calculated by Raman spectra in Figure S2 [20] increased with the increment of HF/Ti ratio from 1 to 3 (42.6% to 97.2%). However, %S of $\text{TiO}_{2\{001\}}$ -4F dropped to 76.3%. This may be due to the stacking phenomenon of $\text{TiO}_{2\{001\}}$ sheet and the collapse of $\text{TiO}_{2\{001\}}$ particles at the side edges (Figure 1(d)). In addition, it was found that the dye loading capacity of $\text{TiO}_{2\{001\}}$ decreased with an increase of %S (Figure 1(g)). This result is in contrast to the conventional understanding that the increase of %S can lead to the higher dye absorption capacity [21]. In our work, grain size seems to be more important factor for increasing dye absorption ability. Thus, 20 wt.% of $\text{TiO}_{2\{001\}}$ was selected to mix in P25 to further increase dye loading capacity of material.

The photovoltaic performance of DSSCs assembled with various $\text{TiO}_{2\{001\}}$ as a photoanode was also investigated. The cell configuration of DSSC and its fabrication method are described in Figures S1 and S1.4, respectively. The J - V curves of DSSCs are shown in Figure 2. It was found that the photoanode containing $\text{TiO}_{2\{001\}}$ -2F showed the most promising short-circuit current density (J_{sc} , 8.57 mA/cm²), which results in an enhancement of PCE (4.63%), compared to that of pure P25 (J_{sc} , 6.40 mA/cm² and PCE, 3.20%). The derived parameters, relating to photovoltaic performance of various DSSCs, were summarized in Table 1.

The enhancement of PCE was further supported by the results from photoluminescence spectroscopy (PL). The PL spectra (Figure 3(a)) of all $\text{TiO}_{2\{001\}}$ samples show similar of broad emission peaks in visible light region. Since the red emission band (~600–650 nm), which is related to Ti^{3+} species, was absent, the emission peaks are therefore associated with the defect states generated by oxygen vacancies, creating the shallow trap and deep trap state [22, 23]. The amount of shallow trap and deep trap states plays a significant role in determining e^- mobility of photoanode materials [24]. The shallow trap states, locating near conduction band edge (CB) of $\text{TiO}_{2\{001\}}$, can effectively capture photoexcited e^- via the hopping mechanism. This can increase the amount of effective e^- and eventually retard charge recombination. In contrast, the deep trap states located at deeper energy can permanently trap the photoexcited e^- , promoting the e^- - h^+ recombination. The PL spectra were deconvoluted at 460 nm and 510–555 nm, corresponding to a shallow trap (blue emission) and a deep trap state (green emission), respectively [25] (SI Figure S3). Interestingly, the $\text{TiO}_{2\{001\}}$ -2F has the highest areal emission ratio ($A_{\text{shallow}}/A_{\text{deep}}$) of 1.13, as shown in Figure 3(b). This result is also consistent with an increase of J_{sc} value. In this study, it was believed that the presence of shallow trap sites may be caused by the unsaturated bonds (5c-Ti and 2c-O) [26]. However, the $\text{TiO}_{2\{001\}}$ -3F, which has the highest %S value (97.24%), provided a lower J_{sc} and fill factor (FF). This could be due to high F^- concentration, which was incorporated into TiO_2 lattice, forming -Ti-F-Ti- bonds, leading to the formation of defect at deep in $\text{TiO}_{2\{001\}}$ crystal [27].

The electrochemical impedance spectroscopy (EIS) was conducted to further gain insight into the charge transport dynamics of DSSCs fabricated with various $\text{TiO}_{2\{001\}}$. Because of low charge transfer resistance at the Pt electrode (R_{CE}) (SI Figure S4), the Nyquist plots (Figure 3(c)) show only the 2nd semicircle, which represents charge recombination resistance between photoanode and electrolyte interface (R_{rec}) [28]. The radius of the semicircle decreased with respect to the increase of HF content, resulting in a higher charge recombination rate. Moreover, the series resistances (R_s) of DSSCs [29] were increased with an increased HF concentration. This directly corresponds to the increased deep trap state in $\text{TiO}_{2\{001\}}$ [30]. Interestingly, the DSSC fabricated by using $\text{TiO}_{2\{001\}}$ -2F as a photoanode has the higher charge recombination resistance (200.51 Ω) and lower series resistance (15.62 Ω) compared to the other samples. Furthermore, Bode plots (Figure 3(d)) and the parameters relating to the impedance properties (Table 2) suggest that the $\text{TiO}_{2\{001\}}$ -2F can significantly enhance the electron lifetime ($\tau_n = 1/2\pi\omega_{\text{max}}$, 1.599 ms) and improve the electron transport time ($\tau_s = R_s C_\mu$, 0.125 ms). Consequently, the charge collection efficiency ($\eta_c = (1 + \tau_s/\tau_n)^{-1}$, 92.77%) of DSSC was significantly increased [31–33]. Based on the above results, the $\text{TiO}_{2\{001\}}$ -2F was selected to further dope with nonmetallic atoms to enhance the light harvesting efficiency of material.

The doping of $\text{TiO}_{2\{001\}}$ -2F with N and S atoms (designated as N-, S- $\text{TiO}_{2\{001\}}$ -2F) was carried out to enhance light harvesting efficiency of $\text{TiO}_{2\{001\}}$ [34] (the method was

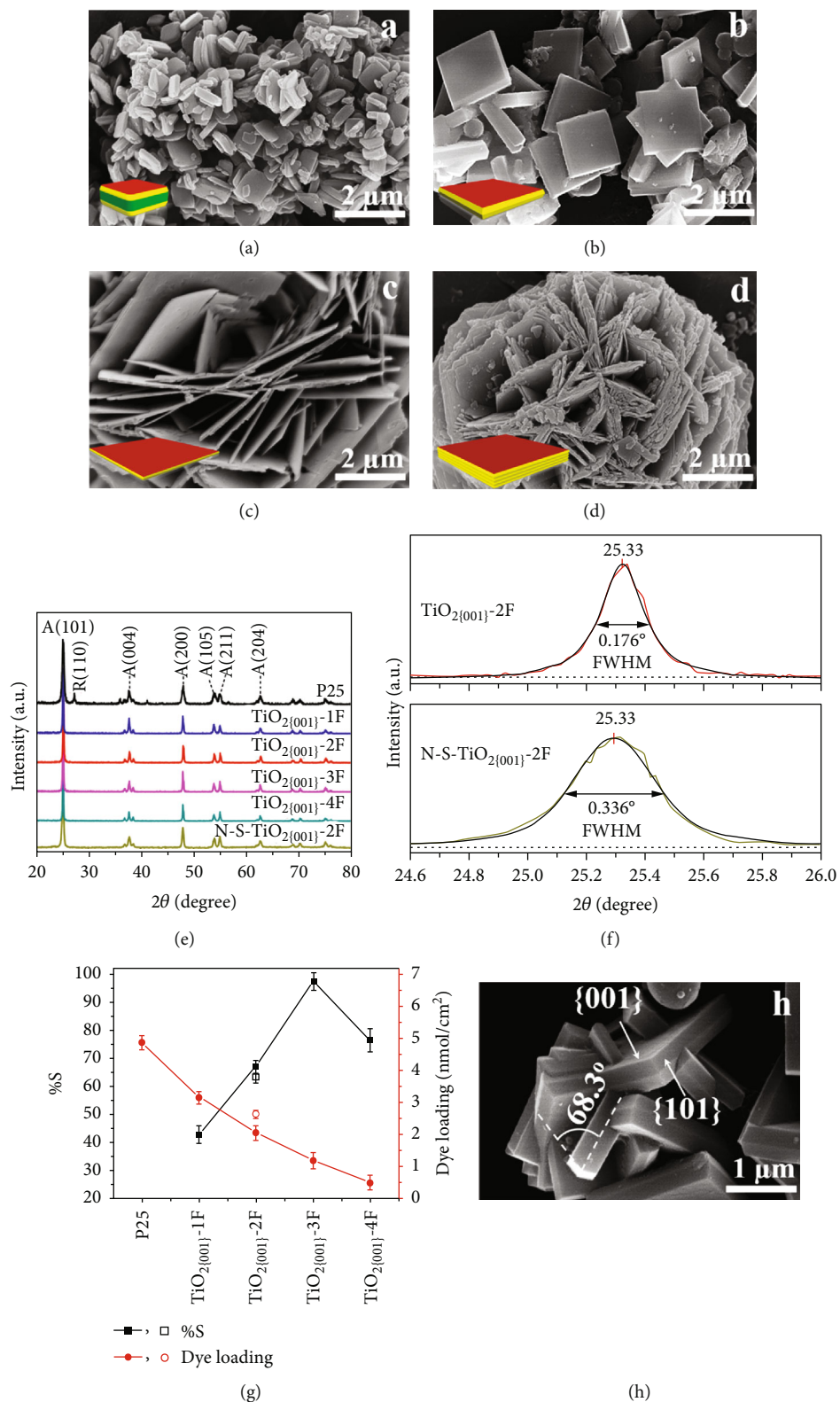


FIGURE 1: (a–d) SEM images showing morphological transformation of TiO_2 crystals when the HF/Ti ratios were varied from 1 to 4, respectively. (e) XRD of various $\text{TiO}_2\{001\}$. (f) Percentage of {001} facet (%S) and dye loading capacity of various $\text{TiO}_2\{001\}$ (filled) and N-, S- $\text{TiO}_2\{001\}$ -2F (blank). (g) The SEM image of N-, S- $\text{TiO}_2\{001\}$ -2F.

described in S1.2). From SEM image (Figure 1(h)), the particle size of N-, S- $\text{TiO}_2\{001\}$ -2F does not change compared to $\text{TiO}_2\{001\}$ -2F. The XRD result (Figure 1(e)) showed that the

N-, S- $\text{TiO}_2\{001\}$ -2F was perfectly indexed to anatase phase and the full width at half maximum (FWHM) at (101) was increased compared to the undoped sample (Figure 1(f)).

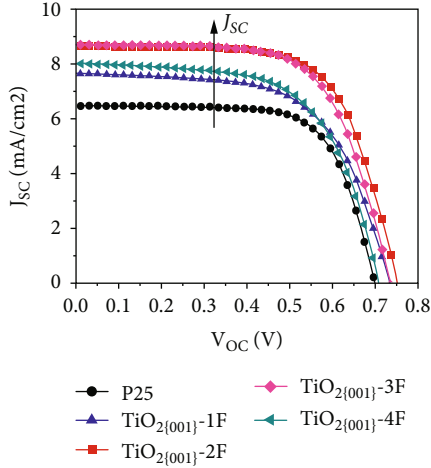


FIGURE 2: J - V curves of DSSCs containing various $\text{TiO}_{2\{001\}}$ (20 wt. %) mixed P25 as photoanode.

TABLE 1: Photovoltaic parameters of DSSCs assembled with 20 wt. % of various $\text{TiO}_{2\{001\}}$ mixed with P25 as photoanode.

Photoanodes	J_{sc} (mA/cm^2)	V_{oc} (V)	FF (a.u.)	PCE (%)	Stdv.
$\text{TiO}_{2\{001\}}$ -1F	7.60	0.74	0.66	3.71	± 0.255
$\text{TiO}_{2\{001\}}$ -2F	8.57	0.75	0.72	4.63	± 0.204
$\text{TiO}_{2\{001\}}$ -3F	8.55	0.74	0.69	4.35	± 0.162
$\text{TiO}_{2\{001\}}$ -4F	7.95	0.71	0.68	3.86	± 0.322
P25	6.40	0.70	0.71	3.20	± 0.183

This suggests that the dopants can reduce the grain size of the $\text{TiO}_{2\{001\}}$ [34], resulting an increase of dye loading capacity (blank red circle in Figure 1(g)). Furthermore, the successful incorporation of N and S atoms in $\text{TiO}_{2\{001\}}$ lattice was also confirmed by the XPS spectra, as shown in Figures S5a and S5b. However, we found that the %S of N-, S- $\text{TiO}_{2\{001\}}$ -2F decreased (blank black square in Figure 1(g)). This implies that the incorporation of N and S atoms in $\text{TiO}_{2\{001\}}$ lattice might affect the vibrational signal of O-Ti-O (E_g and A_{1g} bands), which was corresponded to the blue shifted and broader of E_g band in Raman spectrum of N-, S- $\text{TiO}_{2\{001\}}$ -2F (SI Figure S2, inset). This suggests that the local lattice was changed due to the oxygen vacancies, forming by the incorporation of nonmetallic atoms [35].

The N-, S-doped reduced graphene oxide (rGO) was used to improve electron collection efficiency of DSSC because of its high electrical conductivity [36]. The graphene oxide (GO) used as precursor of rGO was successfully prepared by using modified Hummer's method under low temperature assisted with preexfoliation condition (rGO-(PreEx/LT)). The N-, S-doped rGO (N-, S-rGO-(PreEx/LT)) was then synthesized by the wet chemical reduction method. More details about their synthesis were described in SI S1.3.

Figure 4(a) illustrates the schematic of the synthesized GOs together with the resulting morphologies of the materials characterized by SEM technique. It was found that GO-(PreEx/LT) (Figure 4(d)) has smooth surface, thin sheet,

and large lateral size. In addition, from the XRD pattern (Figure 4(f)), the GO-(PreEx/LT) has larger d -spacing along (001) direction (d_{001} , 8.67 Å), larger average crystallite size (L_{001} , 9.63 nm), larger average diameter of stacking layers (D_A , ~24 nm), and higher number of layer of graphene sheets (N_L , 12 layers) compared to other GOs [37] (see Table S2 for more calculated data). Moreover, to observe the quality of GOs, the structural changes, defects, and disorders of the GO samples were further investigated by Raman spectroscopy [38]. As shown in Figure 4(g), the 1st-order scattering region [39] of various GOs exhibits D band (1354–1364 cm^{-1}) and G band (1593–1603 cm^{-1}), which represent the disordered of graphitic structure and in-plane sp^2 C=C stretching mode, respectively. The intensity ratio of I_D/I_G of GO-(PreEx/LT) (0.84) is lower than that of GO-(HT) (0.90), indicating the larger of sp^2 graphitic domain with less defects. These indicate that GO-(PreEx/LT) provides better quality of exfoliated graphene sheet.

The successful formation of oxidized GO can be confirmed by FTIR spectra (Figure 5(a)). Basically, four peaks of $\nu(\text{O-H})$ (~3400 cm^{-1}), $\nu(\text{C=O})$ (1719–1731 cm^{-1}), C=C of unoxidized sp^2 graphitic domain (1564–1620 cm^{-1}), and C-O (949–1405 cm^{-1}) vibration are presented in all GO samples [40]. The FTIR data of GO products were fit to perform quantitative analysis of oxygen-containing groups, as shown in Equation S2 [41]. It was found that the overall oxygen-related bond (ORB) of GO-(PreEx/LT) (82.5%) is greater than those of GO-(LT) (77.4%) and GO-(HT) (61.3%). This reveals that the GO synthesized by low temperature assisted with pre-exfoliation process gave higher oxidation degree. The peak position and calculated peak area of each functional groups of various GOs was summarized in Table S3.

Furthermore, UV-visible absorption spectra (UV-vis), as shown in Figure 5(b), present the peaks at 238–245 nm, corresponding to the $\pi \rightarrow \pi^*$ electronic transitions of aromatic conjugated system of sp^2 domain (C=C) bonds, while the weak shoulders at around 300–311 nm assigned to the $n \rightarrow \pi^*$ transitions present the oxygen containing groups, locating at the edge and basal plane of graphene sheet [42, 43]. From these results, the relative normalized intensity of absorption peak at $n \rightarrow \pi^*$ band of GO-(PreEx/LT) is relatively high and the position of $\pi \rightarrow \pi^*$ band of GO-(PreEx/LT) (238 nm) is blue shifted as compared to GO-(LT) (inset in Figure 5(b)). This means that the GO-(PreEx/LT) has high-oxidation degree, which is consistent with FTIR result [44]. Thus, GO-(PreEx/LT) was considered to be a suitable precursor for N-, S-codoped rGO.

The GO-(PreEx/LT) was further used to prepare N-, S-doped reduced graphene oxide (N-, S-rGO-(PreEx/LT)) to improve electrical conductivity. The morphology of N-, S-rGO-(PreEx/LT) is shown in Figure 4(e). The presence of many wrinkled, rippled, and scrolled graphene sheets were observed. Moreover, the XRD pattern of N-, S-rGO-(PreEx/LT) (Figure 4(f)) clearly shows a broad diffraction peaks at $\sim 24^\circ$, corresponding to the (002) diffraction plane of rGO (JCPDS Card No.75-1621), which shifted to higher diffraction angle compared with (001) diffraction angle of GO-(PreEx/LT). This can be confirmed that the GO was successfully reduced, resulting in lower d -spacing.

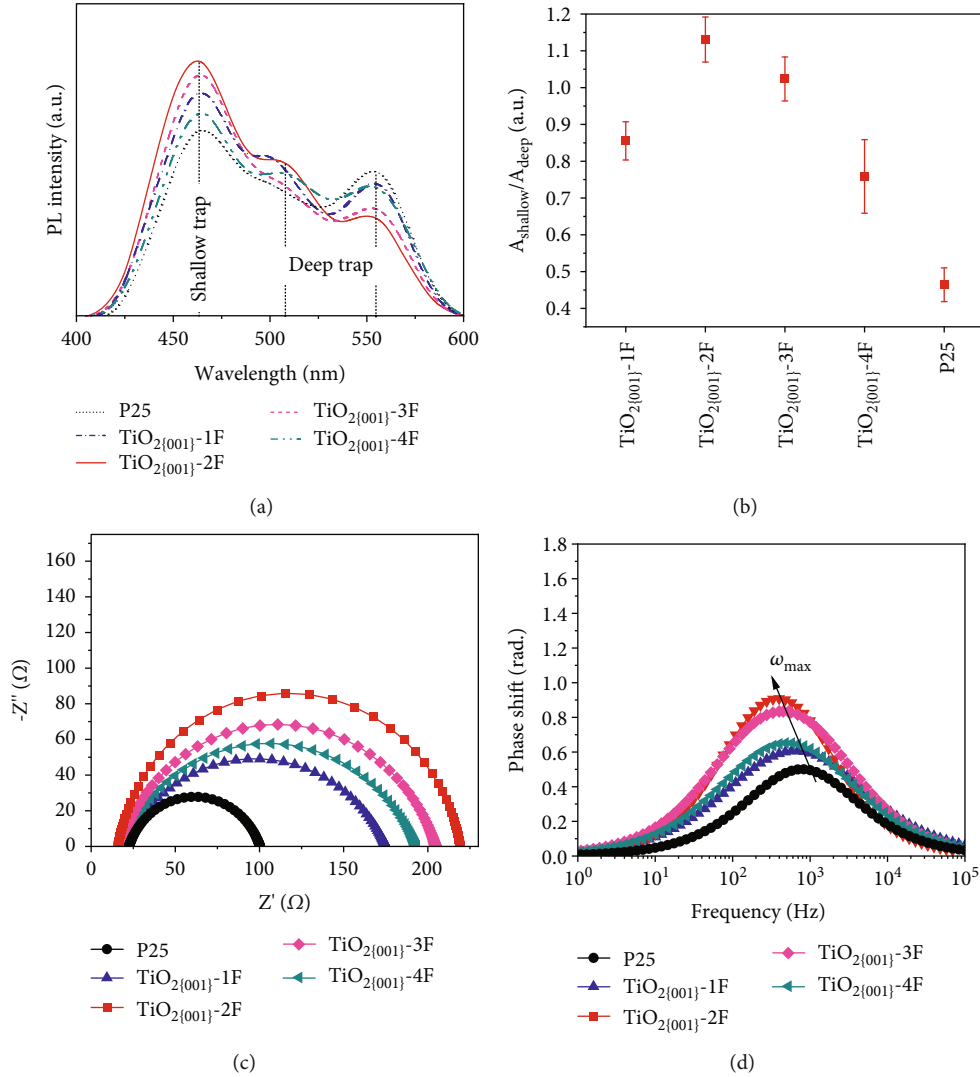


FIGURE 3: (a) PL spectra and (b) the plot of areal emission ratio ($A_{\text{shallow}}/A_{\text{deep}}$) of various $\text{TiO}_{2\{001\}}$. (c) Nyquist plots and (d) Bode phase plots of DSSCs fabricated by using various $\text{TiO}_{2\{001\}}$ as a photoanode. The inset in (c) is the equivalent circuit of DSSC cell configuration, where R_s , R_{CE} , and R_{rec} refer to series resistance, charge transfer resistance at Pt counter electrode, and charge recombination resistance at $\text{TiO}_2/\text{electrolyte}$ interface, respectively. The parameters $CPE1/CPE2$ and W_s denote constant phase elements and Warburg impedance, respectively.

TABLE 2: EIS parameters of DSSCs fabricated with various photoanodes.

Photoanode	R_s (Ω)	R_{rec} (Ω)	C_μ (μF)	τ_n (ms)	τ_s (ms)	η_c (%)
TiO ₂ {001}-1F	19.87	155.68	7.52	1.171	0.149	88.68
TiO ₂ {001}-2F	15.62	200.51	7.98	1.599	0.125	92.77
TiO ₂ {001}-3F	17.35	187.53	8.16	1.530	0.141	91.53
TiO ₂ {001}-4F	18.46	174.82	7.91	1.383	0.146	90.45
P25	22.42	77.86	6.72	0.523	0.151	77.64

R_s : series resistance; R_{rec} : charge recombination resistance; C_μ : chemical capacitance; τ_n : e^- lifetime; τ_s : e^- transport time; η_c : charge collection efficiency.

To assure the successful reduction, changes in chemical structure of N-, S-rGO-(PreEx/LT) after reduction process were monitored by using FTIR. The absence of oxygen-containing groups in FTIR spectra (Figure 5(a)) and the red shifted of $\pi \rightarrow \pi^*$ band referred to aromatic conjugated sys-

tem of C=C in UV-vis spectra (Figure 5(b)) were noted. These indicate that the electronic conjugation within graphene sheet (sp^2) is restored after doping and reduction [45]. In addition, the quality of synthesized N-, S-rGO-(PreEx/LT) was examined by using Raman spectroscopy

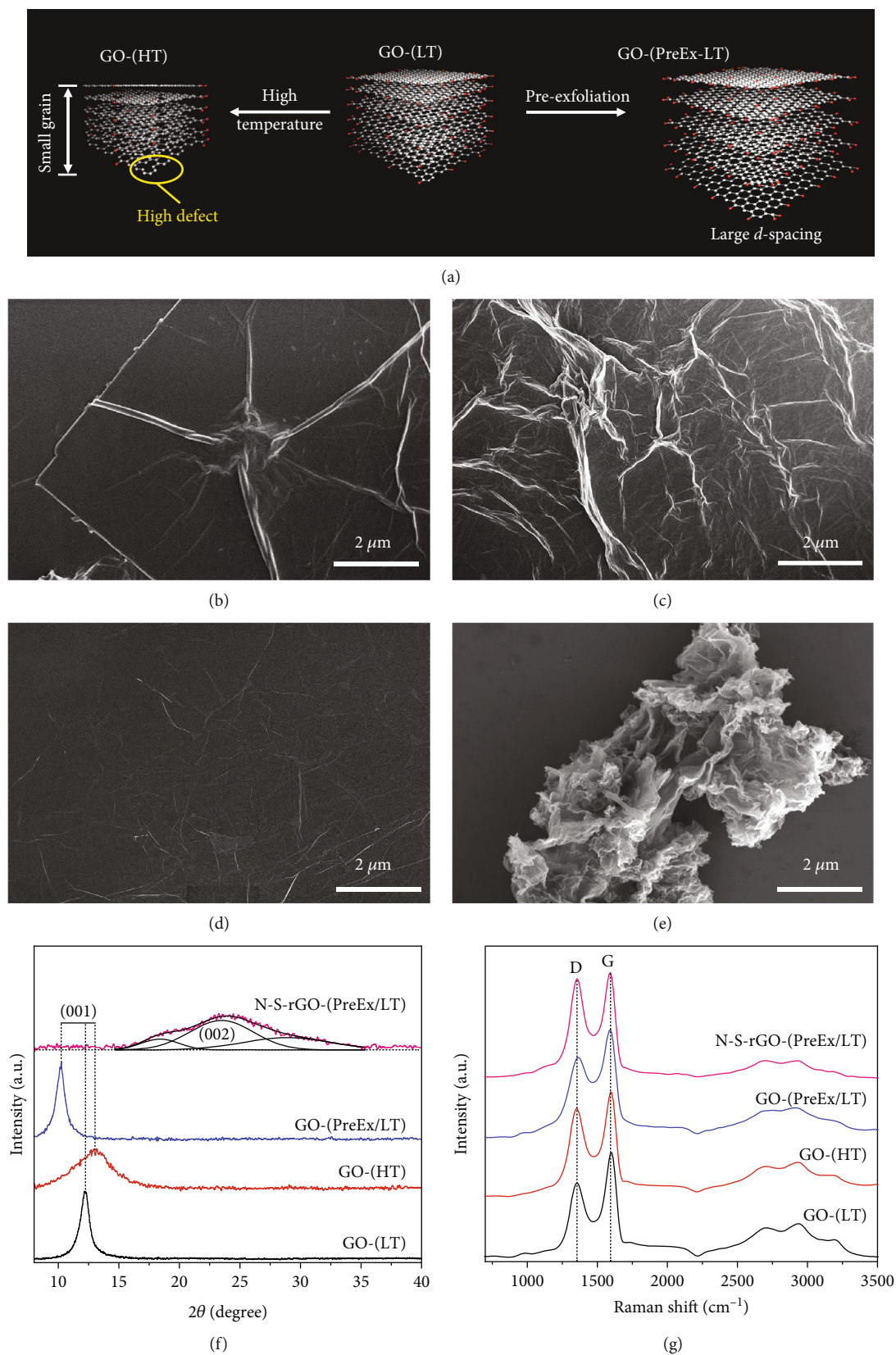


FIGURE 4: (a) Schematic illustration of various synthetic routes and (b–d) SEM images showing the corresponding morphology GO products, respectively. (e) XRD pattern and (f) Raman spectra of various GOs and N-, S-rGO-(PreEx/LT).

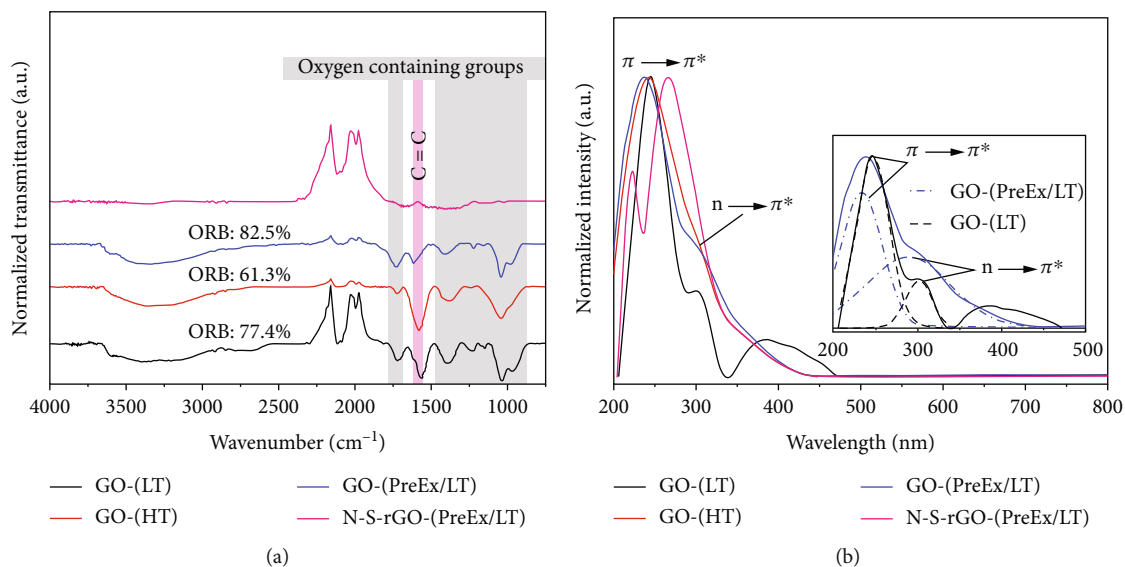


FIGURE 5: (a) FTIR and (b) UV-vis spectra of various GOs derived from different synthesis conditions.

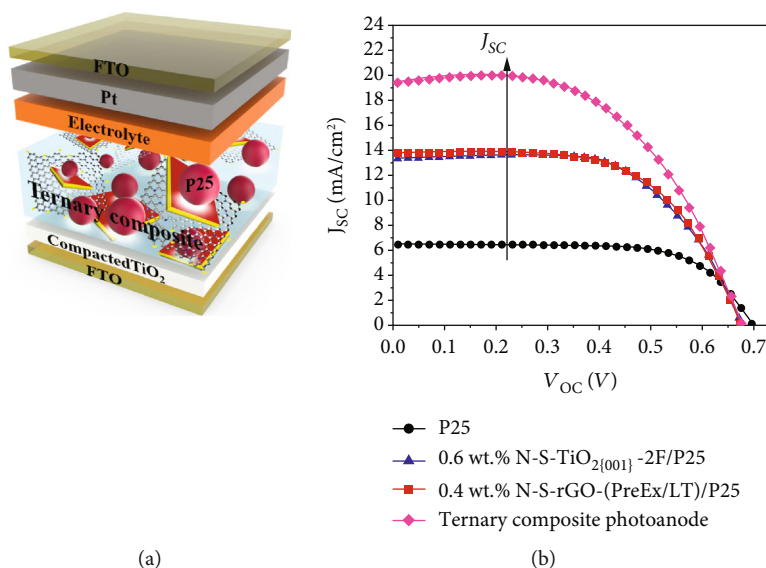


FIGURE 6: (a) The cell configuration of DSSC fabricated with ternary composite photoanode. (b) J - V curves of DSSCs fabricated with various photoanodes.

(Figure 4(g)). I_D/I_G values of the N-, S-rGO-(PreEx/LT) (0.98) was greater than that of GO-(PreEx/LT) (0.84), indicating that N and S atoms can cause some defects or disorders in the graphene structure.

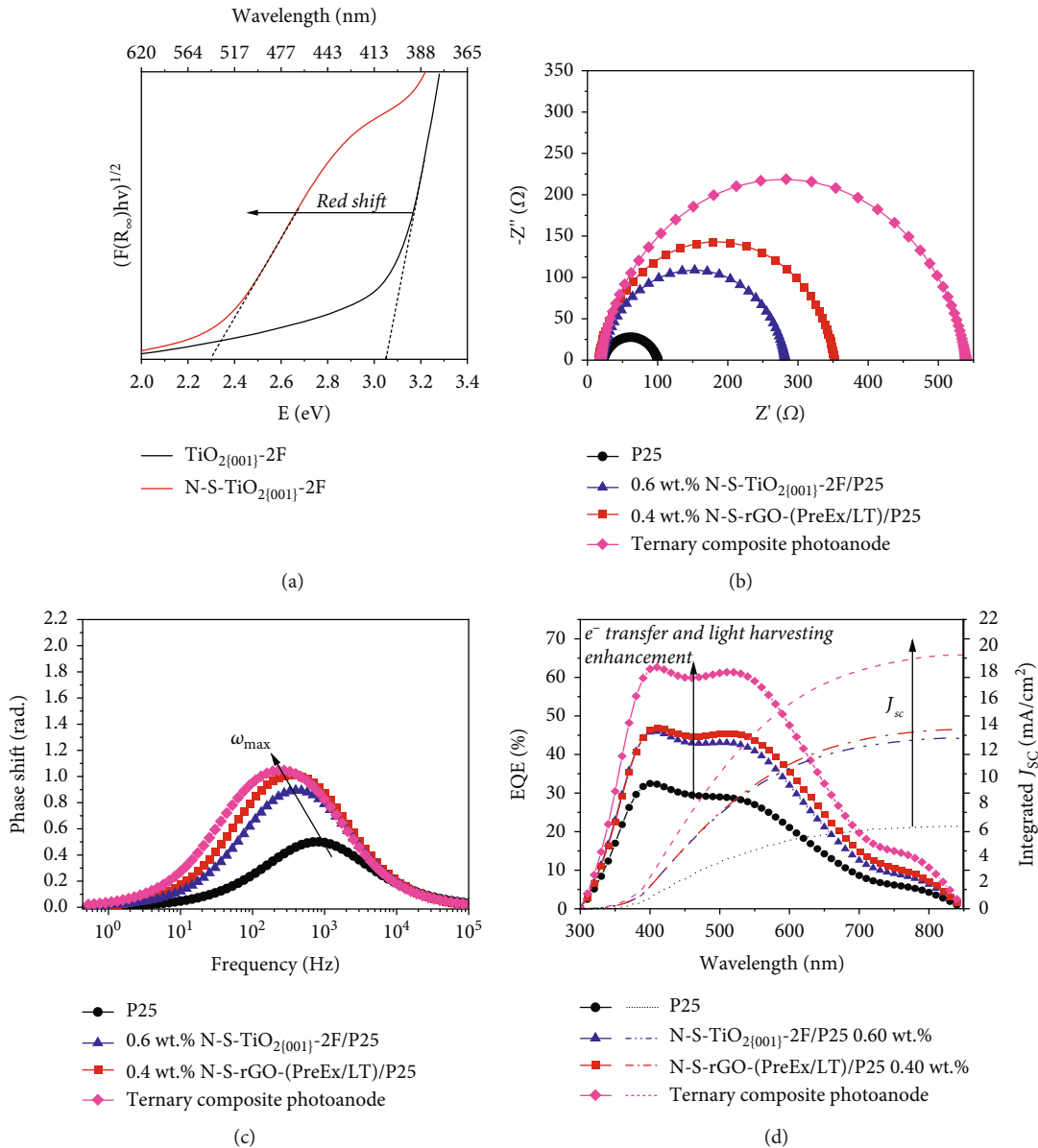
In this part, the N-, S-TiO₂₍₀₀₁₎-2F and N-, S-rGO-(PreEx/LT) with different ratios in P25 were utilized as a composite photoanode. The J - V curves, as seen in Figures S7a and S7b, showed the significant enhancement in the J_{sc} up to 13.10 mA/cm² (6.55% PCE), and 13.77 mA/cm² (6.09% PCE) can be found in two devices containing 0.6 wt.% of N-, S-TiO₂₍₀₀₁₎-2F in P25 and 0.4 wt.% of N-, S-rGO-(PreEx/LT) in P25, respectively (the photovoltaic parameters of DSSCs fabricated by various photoanodes can be found in Table S4). From these optimum contents, weight ratio between N-, S-TiO₂₍₀₀₁₎-2F and N-, S-rGO-

(PreEx/LT) was fixed at 3:2 and then this component was mixed with P25 in various contents to make the ternary composite photoanode (Figure 6(a)).

Interestingly, as seen in Figure S7c, 1.0 wt.% of the mixture of N-, S-TiO₂₍₀₀₁₎-2F and N-, S-rGO-(PreEx/LT) (3:2 by wt.) in P25 based ternary composite photoanode boosted the PCE up to 8.62%, which was about 2.7 times enhancement compared to the photoanode made of pure P25 (3.20%). In addition, the large improvement of J_{sc} up to 19.47 mA/cm², which was around 3 times enhancement compared to P25 (6.40 mA/cm²) was noticed. This suggests the synergistic cooperation of both N-, S-rGO-(PreEx/LT) and N-, S-TiO₂₍₀₀₁₎-2F in P25. The J - V results and photovoltaic parameters of DSSCs fabricated by various photoanodes were summarized in Figure 6(b) and Table 3, respectively.

TABLE 3: Photovoltaic parameters of DSSCs assembled with various photoanodes.

Photoanodes	J_{sc} (mA/cm ²)	V_{oc} (V)	FF (a.u.)	PCE (%)	Stdv.
Pure P25	6.40	0.70	0.71	3.20	±0.183
0.6 wt.% N-, S-TiO ₂ {001}-2F/P25	13.10	0.65	0.77	6.55	±0.109
0.4 wt.% N-, S-rGO (PreEx/LT)/P25	13.77	0.60	0.74	6.09	±0.209
1.0 wt.% ternary composite photoanode	19.47	0.69	0.64	8.62	±0.072

FIGURE 7: (a) Band gap energy calculated by modified Kubelka-Munk function of N-, S-TiO₂{001}-2F and TiO₂{001}-2F. (b) Nyquist plots, (c) Bode phase plots, and (d) EQEs of DSSCs fabricated with various photoanodes.

The UV-vis absorption spectra should be considered to investigate the enhancement of PCE. As shown in Figure 7(a), the Kubelka-Munk plot of N-, S-TiO₂{001}-2F exhibited a remarkable red shift (2.3 eV) compared to

that of TiO₂{001}-2F (3.05 eV). This suggests that N-, S-TiO₂{001}-2F could harvest more proportion of sunlight compared to that of undoped sample, resulting in an enhanced density of photoexcited e⁻ in DSSC cell as clearly

TABLE 4: EIS parameters of DSSCs fabricated with various photoanodes.

Photoanode	R_s (Ω)	R_{rec} (Ω)	C_μ (μF)	τ_n (ms)	τ_s (ms)	η_c (%)
P25	22.42	77.86	6.72	0.52	0.15	77.64
N-, S-TiO ₂ {001}-2F	20.21	261.89	6.54	1.71	0.13	92.84
N-, S-rGO-(PreEx/LT)	15.54	335.60	7.78	2.61	0.12	95.57
Ternary composite	12.34	520.95	8.24	4.29	0.10	97.69

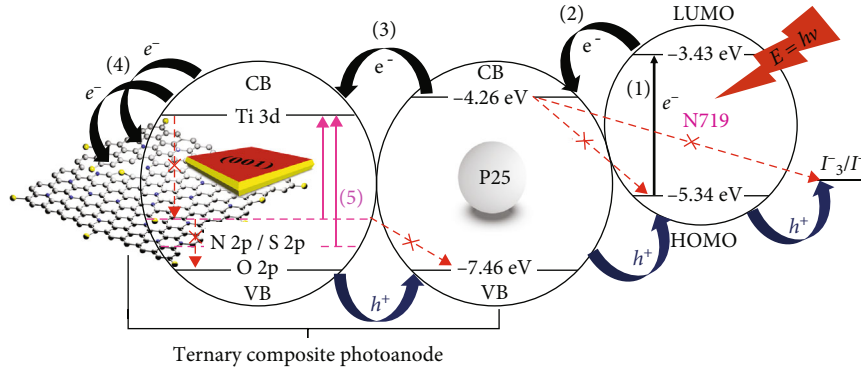


FIGURE 8: Schematic diagram demonstrating proposing the photogenerated charges transfer process of DSSC fabricated with ternary composite photoanode.

indicated by the increased J_{sc} values from 8.57 mA/cm² (TiO₂{001}-2F) to 13.10 mA/cm². Furthermore, the electrochemical impedance spectra (EIS) of DSSC fabricated with various composite photoanodes were recorded. The Nyquist and Bode phase plots are illustrated in Figures 7(b) and 7(c), respectively, and the calculated impedance parameters are summarized in Table 4. The results show that R_s of DSSC was significantly reduced by applying the N-, S-rGO-(PreEx/LT) as photoanode ($R_s = 15.54\Omega$). This indicates that the N-, S-rGO-(PreEx/LT) can effectively improve electrical conductivity of DSSC cell, resulting in a lower R_{rec} (335.60 Ω), a faster e^- transport time (τ_s) (0.12 ms), and a higher e^- lifetime (τ_n) (2.61 ms) as compared to the other photoanodes.

Surprisingly, for ternary composite photoanodes, the lowest R_s (12.34 Ω) and the highest R_{rec} (520.95 Ω) values were achieved (Table 4). Moreover, the frequency at maximum ω_{max} in Bode phase plot of DSSC fabricated by using the ternary composite photoanode was shifted to the lower frequency region. Therefore, from these results, the ternary composite photoanode not only shows faster e^- transport time ($\tau_s = 0.10$ ms) but also exhibited longer e^- lifetime ($\tau_n = 4.29$ ms) as compared to all samples, resulting in the highest charge collection efficiency (η_c) (97.69%).

The enhanced external quantum efficiency (EQE) was observed in N-, S-TiO₂{001}-2F/P25, N-, S-rGO-(PreEx/LT)/P25, and ternary composite photoanode. The EQE (Figure 7(d)) of DSSC fabricated by P25 photoanode has a maximum value of 32.5% and 27.75% at wavelengths 400 nm and 520 nm, respectively. The EQE increase along the whole range of its adsorbed wavelength after 0.6 wt.% of N-, S-TiO₂{001}-2F/P25 was applied. This evidence clearly suggests that the N-, S-TiO₂{001}-2F acts as e^- enricher, leading to an increase of J_{sc} value. In addition, when 0.4 wt.% of

N-, S-rGO-(PreEx/LT) in P25 was introduced into the DSSC, the EQE was also enhanced. This can be described to the improvement of charges transport process through the enhancement of e^- extraction and e^- mobility. Interestingly, EQE was enormously enhanced after addition of ternary composite photoanode (raised to 63%). This result clearly confirms the synergistic effect between e^- enricher (N-, S-TiO₂{001}-2F) and e^- extractor (N-, S-rGO-(PreEx/LT)). The J_{sc} derived from the integration of EQE data were 6.32, 12.99, 13.63, and 19.31 mA/cm² for P25, 0.60 wt.% N-, S-TiO₂{001}-2F/P25, 0.40 wt.% N-, S-rGO-(PreEx/LT)/P25, and ternary composite photoanode, respectively. These are closed to J_{sc} derived by photovoltaic results.

Finally, the proposed charges transfer mechanism of DSSC fabricated using ternary composite photoanode can be described in terms of cascade energy diagram as shown in Figure 8. When dye molecule absorbs the light, the e^- is excited (1) and transferred to the CB of P25 (2). The e^- at this state can move to CB of N-, S-TiO₂{001}-2F (3) via e^- hopping mechanism, and it can be further extracted by N-, S-rGO-(PreEx-LT), which acts as e^- extractor, through the external circuit performing work (4). Moreover, the N-, S-TiO₂{001}-2F as the e^- enricher can be easily excited by visible light (5) (pink arrow in the first circle), resulting in high density of photoexcited e^- . However, photoexcited e^- might be deactivated and recombined (red arrow in all circles). Thus, the combination of e^- extractor can help to quickly extract the photoexcited e^- before the recombination could take place.

3. Conclusions

Nitrogen-sulfur-doped TiO₂ with exposed {001} facet (N-, S-TiO₂{001}-2F) and nitrogen-sulfur-doped reduced graphene

oxide (N-, S-rGO-(PreEx/LT)) were successfully synthesized via hydrothermal and modified Hummer's method followed by the wet chemical reduction process, respectively. The photovoltaic device containing ternary composite photoanode, made from a combination of 1.0 wt.% of N-, S-TiO₂{001}-2F/N-, S-rGO-(PreEx/LT) (3:2 by wt.) and P25, showed the highest power conversion efficiency (PCE) value of 8.62%, which is 2.7 times greater than that of device employing P25 as the photoanode (3.20%). The above effect was ascribed to the large enhancement of J_{sc} value of the former system (19.47 mA/cm²) which is about 3.0 times higher than that of the latter (6.40 mA/cm²). Overall, this study demonstrated the synergistic effect between e⁻ enricher (N-, S-TiO₂{001}-2F) and e⁻ extractor (N-, S-rGO-(PreEx/LT)), which suppressed the charge recombination and improved the PCE value of the solar cell.

Data Availability

The data used to support the findings of this study are available from the corresponding author upon request.

Conflicts of Interest

The authors declare no conflicts of interest.

Acknowledgments

This work has been supported by the Nanotechnology Center (NANOTEC), NSTDA, and Ministry of Science and Technology, Thailand, through its program of Center of Excellence Network. The financial support provided by King Mongkut's University of Technology Thonburi is through the "KMUTT 55th Anniversary Commemorative Fund" and "the Petchra Pra Jom Klao Doctoral Scholarship." Financial support from NANOTEC (grant number P1652084) is also appreciated.

Supplementary Materials

Details on the materials, grade, and supplier (S1.1), the procedure for synthesis TiO₂{001} facet and its doping with nonmetallic atoms (N and S) (S1.2), the synthesis of GO with various conditions (Table S1) and its doping with nonmetallic atoms (N and S) (S1.3), the DSSC cell architecture and its fabrication method (S1.4), descriptions of the characterization techniques (S1.5), Raman spectra of various TiO₂{001} and percentage of {001} facet calculation (Figure S2), the example of deconvoluted PL spectrum (TiO₂{001}-2F) (Figure S3), the example of Nyquist plot of DSSC fabricated by using pure P25 as photoanode (Figure S4), XPS spectra of N-, S-TiO₂{001}-2F and N-, S-rGO-(PreEx/LT) (Figures S5 and S6, respectively), the summary of parameters obtained from XRD data of various GOs (Table S2), the overall oxygen related bonds (ORB) of various GOs (Table S3), the J - V curves (Figure S7), and the parameters relating the photovoltaic testing of various DSSCs that applied different types of photoanodes (Table S4). (*Supplementary Materials*)

References

- [1] K. Kakiage, Y. Aoyama, T. Yano, K. Oya, J. Fujisawa, and M. Hanaya, "Highly-efficient dye-sensitized solar cells with collaborative sensitization by silyl-anchor and carboxy-anchor dyes," *Chemical Communications*, vol. 51, no. 88, pp. 15894–15897, 2015.
- [2] S. Wanwong, W. Sangkhun, and J. Wootthikanokkhan, "The effect of co-sensitization methods between N719 and boron dipyrromethene triads on dye-sensitized solar cell performance," *RSC Advances*, vol. 8, no. 17, pp. 9202–9210, 2018.
- [3] W. Zhang, Y. Wu, H. W. Bahng et al., "Comprehensive control of voltage loss enables 11.7% efficient solid-state dye-sensitized solar cells," *Energy & Environmental Science*, vol. 11, no. 7, pp. 1779–1787, 2018.
- [4] S. Gnanasekar, P. Kollu, S. K. Jeong, and A. N. Grace, "Pt-free, low-cost and efficient counter electrode with carbon wrapped VO₂(M) nanofiber for dye-sensitized solar cells," *Scientific Reports*, vol. 9, no. 1, p. 5177, 2019.
- [5] B. Tang, H. Yu, W. Huang et al., "Three-dimensional graphene networks and RGO-based counter electrode for DSSCs," *RSC Advances*, vol. 9, no. 28, pp. 15678–15685, 2019.
- [6] S. S. Shin, J. H. Suk, B. J. Kang et al., "Energy-level engineering of the electron transporting layer for improving open-circuit voltage in dye and perovskite-based solar cells," *Energy & Environmental Science*, vol. 12, no. 3, pp. 958–964, 2019.
- [7] P.-A. Cormier, J. Dervaux, N. Szuwarski et al., "Single Crystalline-like and nanostructured TiO₂Photoanodes for dye sensitized solar cells synthesized by reactive magnetron sputtering at glancing angle," *Journal of Physical Chemistry C*, vol. 122, no. 36, pp. 20661–20668, 2018.
- [8] S. So, I. Hwang, J. E. Yoo et al., "Inducing a Nanotwinned grain structure within the TiO₂Nanotubes provides enhanced electron transport and DSSC efficiencies >10%," *Advanced Energy Materials*, vol. 8, no. 33, p. 1800981, 2018.
- [9] N. Fu, Y. Duan, W. Lu et al., "Realization of ultra-long columnar single crystals in TiO₂nanotube arrays as fast electron transport channels for high efficiency dye-sensitized solar cells," *Journal of Materials Chemistry A*, vol. 7, no. 18, pp. 11520–11529, 2019.
- [10] Q. Jiang, X. Zhang, and J. You, "SnO₂: a wonderful electron transport layer for perovskite solar cells," *Small*, vol. 14, no. 31, p. 1801154, 2018.
- [11] B. Zhang, F. Wei, Q. Wu, L. Piao, M. Liu, and Z. Jin, "Formation and evolution of the High-Surface-Energy facets of anatase TiO₂," *Journal of Physical Chemistry C*, vol. 119, no. 11, pp. 6094–6100, 2015.
- [12] X. Liu, G. Dong, S. Li, G. Lu, and Y. Bi, "Direct observation of charge separation on anatase TiO₂ crystals with selectively etched {001} facets," *Journal of the American Chemical Society*, vol. 138, no. 9, pp. 2917–2920, 2016.
- [13] S. Sun, P. Gao, Y. Yang, P. Yang, Y. Chen, and Y. Wang, "N-doped TiO₂ nanobelts with coexposed (001) and (101) facets and their highly efficient visible-light-driven photocatalytic hydrogen production," *ACS Applied Materials & Interfaces*, vol. 8, no. 28, pp. 18126–18131, 2016.
- [14] X. Yan, Z. Xing, Y. Cao et al., "In-situ C-N-S-tridoped single crystal black TiO₂ nanosheets with exposed {001} facets as efficient visible-light-driven photocatalysts," *Applied Catalysis B: Environmental*, vol. 219, pp. 572–579, 2017.
- [15] E. M. Rockafellow, L. K. Stewart, and W. S. Jenks, "Is sulfur-doped TiO₂ an effective visible light photocatalyst

- for remediation?," *Applied Catalysis B: Environmental*, vol. 91, no. 1-2, pp. 554–562, 2009.
- [16] Z. Tian, J. Li, G. Zhu et al., "Facile synthesis of highly conductive sulfur doped reduced graphene oxide sheets," *Physical Chemistry Chemical Physics*, vol. 18, no. 2, pp. 1125–1130, 2016.
- [17] D. Konios, G. Kakavelakis, C. Petridis, K. Savva, E. Stratakis, and E. Kymakis, "Highly efficient organic photovoltaic devices utilizing work-function tuned graphene oxide derivatives as the anode and cathode charge extraction layers," *Journal of Materials Chemistry A*, vol. 4, no. 5, pp. 1612–1623, 2016.
- [18] U. Kanta, V. Thongpool, W. Sangkhun, N. Wongyao, and J. Wootthikanokkhan, "Preparations, characterizations, and a comparative study on photovoltaic performance of two different types of graphene/TiO₂ nanocomposites photoelectrodes," *Journal of Nanomaterials*, vol. 2017, Article ID 2758294, 13 pages, 2017.
- [19] T. Butburee, P. Kotchasarn, P. Hirunsit et al., "New understanding of crystal control and facet selectivity of titanium dioxide ruling photocatalytic performance," *Journal of Materials Chemistry A*, vol. 7, no. 14, pp. 8156–8166, 2019.
- [20] F. Tian, Y. Zhang, J. Zhang, and C. Pan, "Raman spectroscopy: a new approach to measure the percentage of anatase TiO₂ Exposed (001) facets," *Journal of Physical Chemistry C*, vol. 116, no. 13, pp. 7515–7519, 2012.
- [21] J.-D. Peng, P. C. Shih, H. H. Lin et al., "TiO₂ nanosheets with highly exposed (001)-facets for enhanced photovoltaic performance of dye-sensitized solar cells," *Nano Energy*, vol. 10, pp. 212–221, 2014.
- [22] K.-S. Jeon, S.-D. Oh, Y. D. Suh, H. Yoshikawa, H. Masuhara, and M. Yoon, "Blinking photoluminescence properties of single TiO₂ nanodiscs: interfacial electron transfer dynamics," *Physical Chemistry Chemical Physics*, vol. 11, no. 3, pp. 534–542, 2009.
- [23] C. Jin, B. Liu, Z. Lei, and J. Sun, "Structure and photoluminescence of the TiO₂ films grown by atomic layer deposition using tetrakis-dimethylamino titanium and ozone," *Nanoscale Research Letters*, vol. 10, no. 1, 2015.
- [24] Y. Wang, D. Wu, L.-M. Fu, X.-C. Ai, D. Xu, and J.-P. Zhang, "Density of state determination of two types of intra-gap traps in dye-sensitized solar cells and its influence on device performance," *Physical Chemistry Chemical Physics*, vol. 16, no. 23, pp. 11626–11632, 2014.
- [25] B. Choudhury, M. Dey, and A. Choudhury, "Shallow and deep trap emission and luminescence quenching of TiO₂ nanoparticles on Cu doping," *Applied Nanoscience*, vol. 4, no. 4, pp. 499–506, 2014.
- [26] Y.-K. Peng, B. Keeling, Y. Li et al., "Unravelling the key role of surface features behind facet-dependent photocatalysis of anatase TiO₂," *Chemical Communications*, vol. 55, no. 30, pp. 4415–4418, 2019.
- [27] A. M. Czoska, S. Livraghi, M. Chiesa et al., "The nature of defects in fluorine doped TiO₂," *Journal of Physical Chemistry C*, vol. 112, no. 24, pp. 8951–8956, 2008.
- [28] S. Sarker, A. J. S. Ahammad, H. W. Seo, and D. M. Kim, "Electrochemical Impedance Spectra of Dye-Sensitized Solar Cells: Fundamentals and Spreadsheet Calculation," *International Journal of Photoenergy*, vol. 2014, Article ID 851705, 17 pages, 2014.
- [29] L. Tao, Z. Huo, Y. Ding et al., "High-efficiency and stable quasi-solid-state dye-sensitized solar cell based on low molecular mass organogelator electrolyte," *Journal of Materials Chemistry A*, vol. 3, no. 5, pp. 2344–2352, 2015.
- [30] B. Roose, S. Pathak, and U. Steiner, "Doping of TiO₂ for sensitized solar cells," *Chemical Society Reviews*, vol. 44, no. 22, pp. 8326–8349, 2015.
- [31] J. Bisquert, F. Fabregat-Santiago, I. Mora-Seró, G. Garcia-Belmonte, and S. Giménez, "Electron lifetime in Dye-Sensitized solar cells: theory and interpretation of measurements," *Journal of Physical Chemistry C*, vol. 113, no. 40, pp. 17278–17290, 2009.
- [32] J. Nissfolk, K. Fredin, A. Hagfeldt, and G. Boschloo, "Recombination and transport processes in dye-sensitized solar cells investigated under working conditions," *The Journal of Physical Chemistry. B*, vol. 110, no. 36, pp. 17715–17718, 2006.
- [33] S. G. Kim, M. J. Ju, I. T. Choi et al., "Nb-doped TiO₂ nanoparticles for organic dye-sensitized solar cells," *RSC Advances*, vol. 3, no. 37, pp. 16380–16386, 2013.
- [34] Q. Xiang, J. Yu, and M. Jaroniec, "Nitrogen and sulfur co-doped TiO₂ nanosheets with exposed {001} facets: synthesis, characterization and visible-light photocatalytic activity," *Physical Chemistry Chemical Physics*, vol. 13, no. 11, pp. 4853–4861, 2011.
- [35] Y. Guo, T. Guo, J. Chen et al., "Synthesis of C–N–S co-doped TiO₂ mischcrystal with an isobandgap characteristic and its photocatalytic activity under visible light," *Catalysis Science & Technology*, vol. 8, no. 16, pp. 4108–4121, 2018.
- [36] W. Han, L. Chen, W. Song et al., "Synthesis of nitrogen and sulfur co-doped reduced graphene oxide as efficient metal-free cocatalyst for the photo-activity enhancement of CdS," *Applied Catalysis B: Environmental*, vol. 236, pp. 212–221, 2018.
- [37] L. Stobinski, B. Lesiak, A. Malolepszy et al., "Graphene oxide and reduced graphene oxide studied by the XRD, TEM and electron spectroscopy methods," *Journal of Electron Spectroscopy and Related Phenomena*, vol. 195, pp. 145–154, 2014.
- [38] C. Zhu, S. Guo, Y. Fang, and S. Dong, "Reducing sugar: new functional molecules for the green synthesis of graphene nanosheets," *ACS Nano*, vol. 4, no. 4, pp. 2429–2437, 2010.
- [39] A. C. Ferrari and D. M. Basko, "Raman spectroscopy as a versatile tool for studying the properties of graphene," *Nature Nanotechnology*, vol. 8, no. 4, pp. 235–246, 2013.
- [40] V. Țucureanu, A. Matei, and A. M. Avram, "FTIR spectroscopy for carbon family study," *Critical Reviews in Analytical Chemistry*, vol. 46, no. 6, pp. 502–520, 2016.
- [41] J. Guerrero-Contreras and F. Caballero-Briones, "Graphene oxide powders with different oxidation degree, prepared by synthesis variations of the Hummers method," *Materials Chemistry and Physics*, vol. 153, pp. 209–220, 2015.
- [42] Q. Lai, S. Zhu, X. Luo, M. Zou, and S. Huang, "Ultraviolet-visible spectroscopy of graphene oxides," *AIP Advances*, vol. 2, no. 3, p. 032146, 2012.
- [43] S. K. Cushing, W. Ding, G. Chen et al., "Excitation wavelength dependent fluorescence of graphene oxide controlled by strain," *Nanoscale*, vol. 9, no. 6, pp. 2240–2245, 2017.
- [44] Y. Zhou, Q. Bao, L. A. L. Tang, Y. Zhong, and K. P. Loh, "Hydrothermal dehydration for the 'green' reduction of exfoliated graphene oxide to graphene and demonstration of tunable optical limiting properties," *Chemistry of Materials*, vol. 21, no. 13, pp. 2950–2956, 2009.
- [45] R. López and R. Gómez, "Band-gap energy estimation from diffuse reflectance measurements on sol-gel and commercial TiO₂: a comparative study," *Journal of Sol-Gel Science and Technology*, vol. 61, no. 1, pp. 1–7, 2012.